ROTOR BEARING SOLUTIONS INTERNATIONAL, LLC

www.rotorsolution.com

Initial Levitation Testing and Design of Magnetic Bearing System for High Speed Turbo-Aerator

Prepared by:

RBSI Team

Simon Mushi, Brad Nichols, Tim Dimond, Paul Allaire, and Jianming Cao

Kinetic Traction Systems Team

Richard Newark, Nigel Lloyd, Nick Schulze, Brad Billow, Farshad Daneshvar, and Omar Alshahrani

Rotor Bearing Solutions International, LLC
3277 Arbor Trace
Charlottesville, VA 22911

April 15, 2017

Initial Levitation Testing and Design of Magnetic Bearing System for High Speed Turbo-Aerator

Simon MUSHI*, Brad NICHOLS*, Tim DIMOND*, Paul ALLAIRE*, Jianming CAO*, Richard NEWARK**, Nigel LLOYD**, Nick SCHULZE**, Brad BILLOW**, Farshad DANESHVAR** and Omar ALSHAHRANI**

* Rotor Bearing Solutions International, LLC
3277 Arbor Trace, Charlottesville, Virginia 22911, USA
E-mail: paul.allaire@rotorsolution.com

** Kinetic Traction Systems, Inc.
20360 Plummer Street, Chatsworth, California 91311, USA
E-mail: dick.newark@kinetictraction.com

Abstract

This paper concerns the design, construction and initial levitation testing of a full 5-axis magnetic bearing suspension system for an industrial high speed turbo-aerator. The operating speed range of the machine is 16,000 rpm (267 Hz) to 25,000 rpm (417 Hz). The overall turbo aerator configuration is shown and the thrust and radial bearing configurations and design principles are presented. The rotor is a rigid rotor over the operating speed range. The assembled turbo aerator with magnetic bearings is presented with initial test results. The system sensors and power electronics hardware are described in some detail. The casing ping test results are given. The measured PID control results for the rigid rotor for API stability, in terms of AMB system output sensitivity plots show class A operation. Also unbalance rejection control results, with and without the unbalance rejection control, are described.

Key words : Active Magnetic Bearing, Turbo-aerator, Thrust Bearing, Radial Bearing

1. Introduction

Liquid aeration in many industrial processes, such as used in activated wastewater treatment plants, may contribute up to 40 to 60% of the plants overall energy usage. Historically these plants have used positive displacement pumps or rotary compressors for aeration. The high speed turbo-aerator presented in this paper and illustrated in Fig. 1 is expected to reduce electricity costs by up to 30%. The machine is designed to operate at an air flow rate of 112 m^3/min at a pressure of 55 MPa. The operating speed range of the machine is 16,000 rpm (267 Hz) to 25,000 rpm (417 Hz). The turbo-aerator cabinet, containing both the core machine and all supporting power electronics, has dimensions of approximately 2 m high, 1.8 m wide, and 1.8 m in depth. The total mass is approximately 1.9 kg. The machine is driven by a 200 kW, 380/480 volt, three phase motor with forced air cooling. The generator produces approximately 135 kW at peak power.

The turbo-aerator is fully suspended in 5-axes- 2 axes for each of 2 radial bearings, 1 axis for a single thrust bearing- with active magnetic bearings and includes rolling element auxiliary, or back-up, bearings. The core machine assembly is shown in Fig. 2. This shows the assembled aerator volute, motor casing, AMB power cables, and motor leads.

2. Magnetic Thrust Bearing Design

The turbo-aerator is a vertical-axis machine, so the primary load on the thrust bearing is the rotor weight. The designed thrust load is 1,700 N which takes into account both the rotor weight and anticipated fluid loads, multiplied by a factor of safety. The thrust bearing configuration is shown in Fig. 3. Each side of the stator contains an annular coil pack fixed between two annular poles connected through a back iron. Fig. 4 shows a photograph of one side of the thrust bearing stator depicting the coil windings located between the segmented poles.

The thrust bearing stator and disk are composed of solid AISI 4340, a high stength material that allows for high centrifugal stress levels in the thrust disk. The calculated peak stress in the disk is 224 MPa at 27,000 rpm. The thrust stator is segmented, to reduce eddy currents in the stator.

The thrust disk has inner and outer diameters of 102.5 and 165 mm, repectively, and an axial length of 69 mm. Using

a magnetic circuit model, the current gain and open loop stiffness are calculated as k_i = 570 N/A and k_z = - 5,580 N/mm. The coil resistance is 0.36 Ω and the inductance is L=54 mH. As calculated in the magnetic circuit model, a coil current of 7.5 A is required to produce the designed load capacity of 1,700 N. This value is compared to results from both a 2-D and 3-D finite element model which produced 1,625 N and 1,789 N load capacity, repectively. The 2-D FEA model, shown in Fig. 5, predicts only 4% lower load capacity than the magnetic circuit model.

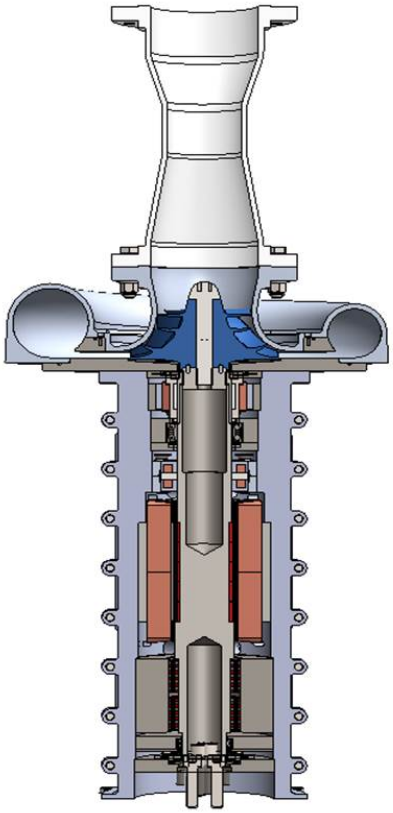

Fig. 1: Cutaway configuration of turbo-aerator supported by 5-axis active magnetic bearing system.

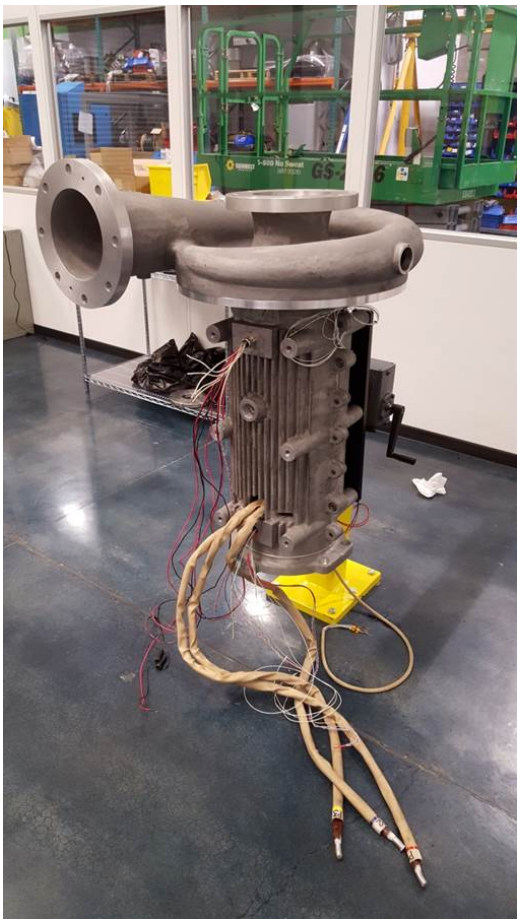

Fig. 2: Cutaway configuration of turbo-aerator supported by 5-axis active magnetic bearing system.

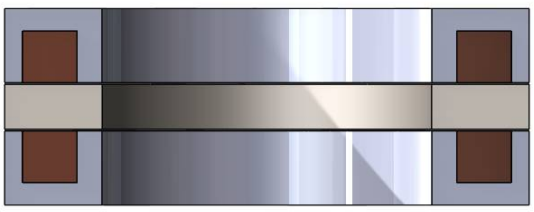

Fig. 3: Thrust bearing configuration with a single coil and two poles on each side of the thrust disk.

Fig. 4: Photograph of the thrust stator showing the segmented poles and the coil winding.

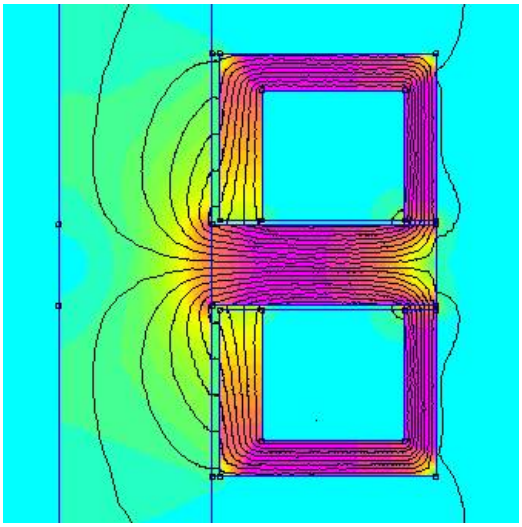

Fig. 5: Magnetic flux density plot of thrust bearing obtained from 2-D FEA analysis.

3. Magnetic Radial Bearing Design

The radial bearings are a 12-pole E-core configuration design as shown in Fig. 6. Since the turbo-aerator is a vertical machine, there is no gravity load on the radial bearings. The primary load is due to the rotor unbalance forces. A photograph of one 12-pole radial bearing with coil leads is shown in Fig. 7.

The bearing stator and rotor are composed of laminated silicon iron materials. The design load capacity is 1000 N, which includes the expected unbalance forces multiplied by a factor of safety. The bearing stator has an inner and outer diameter of 82 and 102.5 mm, repectively, and an axial length of 78 mm. The magnetic circuit model yields a current gain of k_i = 136 N/A and an open-loop stiffness of k_z = - 2,400 N/mm. The coil resistance is 21 Ω and the inductance is L = 3 mH. A 2-D finite element model of the radial bearing is shown in Fig. 8.

A photograph of the upper radial bearing installed in the turbo aerator casing is shown in Fig. 9. A photograph of the lower radial bearing installed in the casing is shown in Fig. 10.

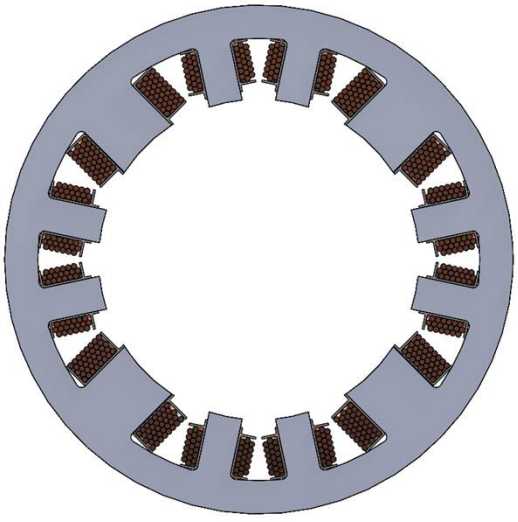

Fig. 6: Diagram of 12-pole radial active magnetic bearing illustrating the E-core configuration.

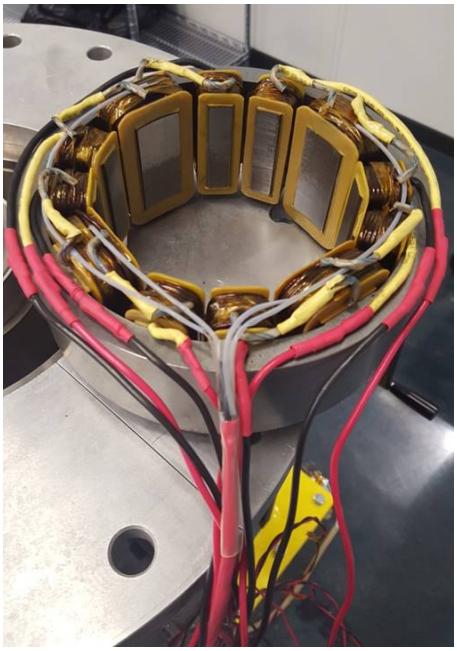

Fig. 7: Pre-instillation photograph of 12-pole E-core radial AMB with leads.

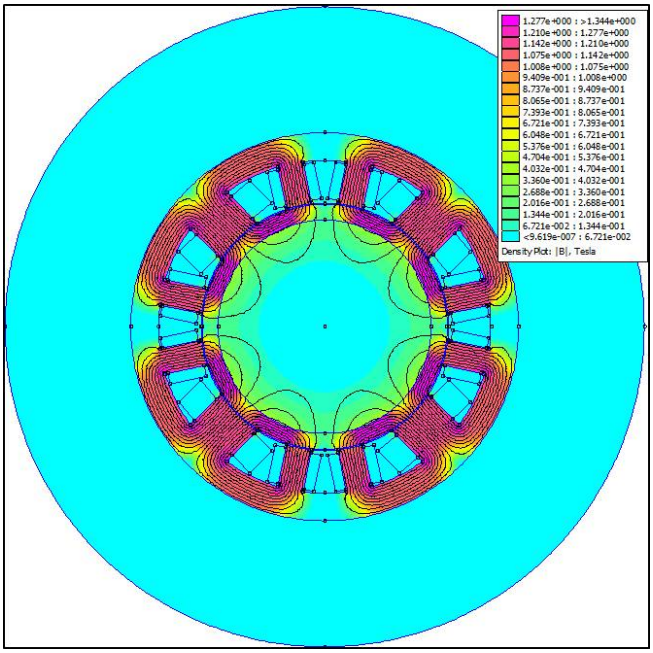

Fig. 8: Magnetic flux density plot of radial bearing obtained from 2-D FEA analysis.

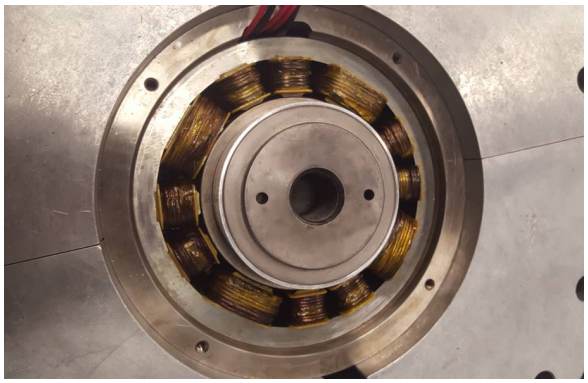

Fig. 9: Upper radial bearing installed in turbo-aerator housing.

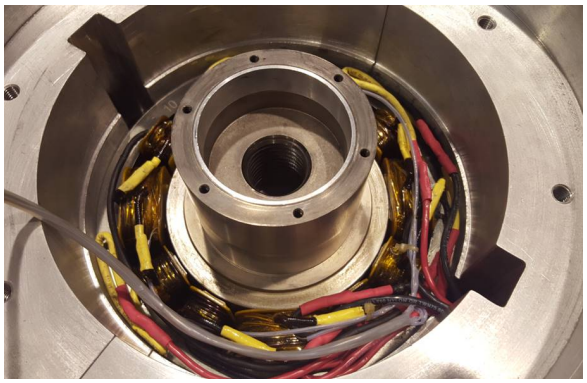

Fig. 10: Upper radial bearing installed in turbo-aerator housing.

4. Rotor Dynamics Critical Speeds and Mode Shapes

A finite element model of the rotor was developed to generate a critical speed map and evaluate the undamped critical speeds and mode shapes of the rotor. Fig. 11 shows the resulting critical speed map while Fig. 12 illustrates the first six undamped mode shapes using expected AMB stiffness values. The first rigid body mode, pictured in blue in both graphics, is located at 2,550 rpm (42.5 Hz), while the second rigid body mode, pictured in red, is located at 3,602 rpm (60 Hz). The first rotor bending mode, pictured in green, is at 41,840 rpm (697 Hz), well above the maximum rotor operating speed of 25,000 rpm (467 Hz). These results indicate that only the first two rigid body modes will be of interest in the AMB system controller as the machine will run through these on the way to the operating speed.

5. Power Electronics Cabinet

The power electronics cabinet is shown in Fig. 13. The electric motor VFD is shown on the left side with a step down transformer below it. The right side of the cabinet contains a 24-volt power supply, Kontron control CPU, amplifier box, and UPS mounted one above another in descending order. Fig. 14 shows a detailed view of the amplifier box containing ten amplifiers, one per control axis, for the 5-axis AMB support system.

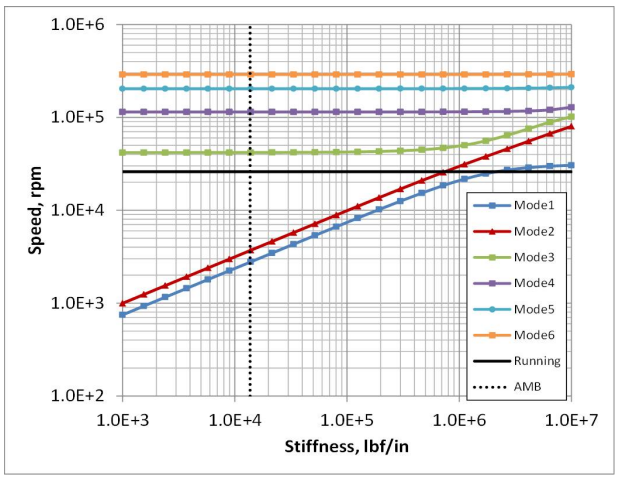

Fig. 11: Rotor critical speed map obtained from 2-D FEA.

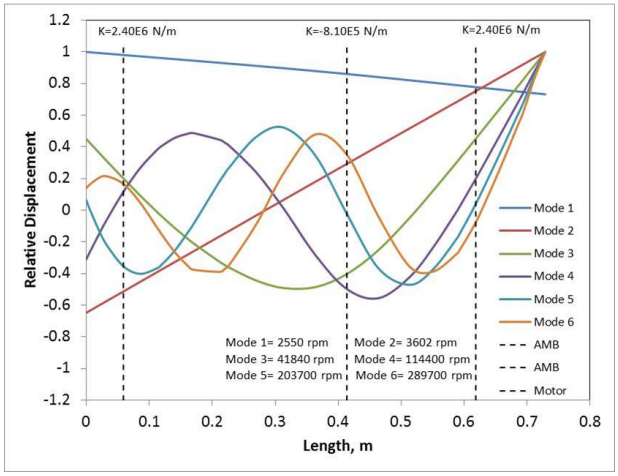

Fig. 12: First six rotor undamped mode shapes.

Fig. 13: Turbo-aerator motor and AMB power electronics cabinet.

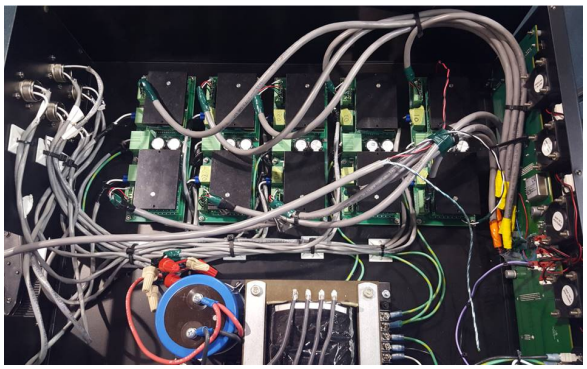

Fig. 14: Turbo-aerator amplfier box with ten amplifiers- two per control axis.

6. Displacement Sensors

Kaman eddy current displacement sensors are used to monitor rotor position for feedback to the controller with two sensors used in differential mode for each control axis. The sensors were tested and calibrated in a simple static test rig as shown in Fig. 15 to determine DC offsets for each control axis. Fig. 16 shows one sensor plate installed in the turbo-aerator casing above the top radial AMB.

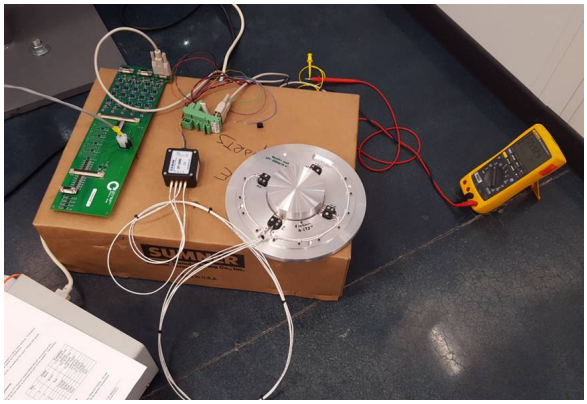

Fig. 15: Two sets of differential eddy-current sensors in test rig to obtain DC offset values.

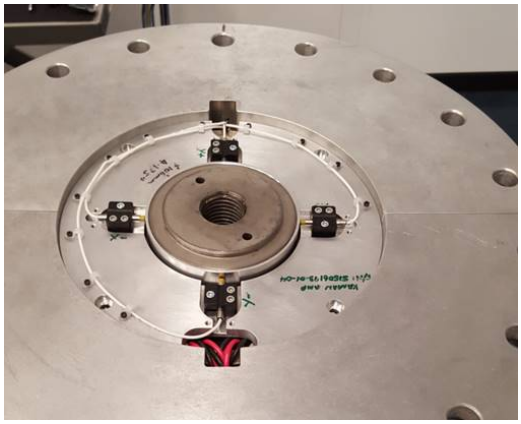

Fig. 16: Sensor plate installed in turbo-aerator casing above top radial AMB.

7. Assembled Turbo-Aerator for Testing

The assembled core machine installed in its cabinet is shown in Fig. 17. The inlet flow venturi is located at the top of the machine above the volute. A cooling shroud is located around the motor casing. The complete assembled unit is shown in Fig. 18 with a discharge pipe exiting the cabinet to the right.

Fig. 17: Core machine installed in cabinet with inlet venturi and cooling shroud.

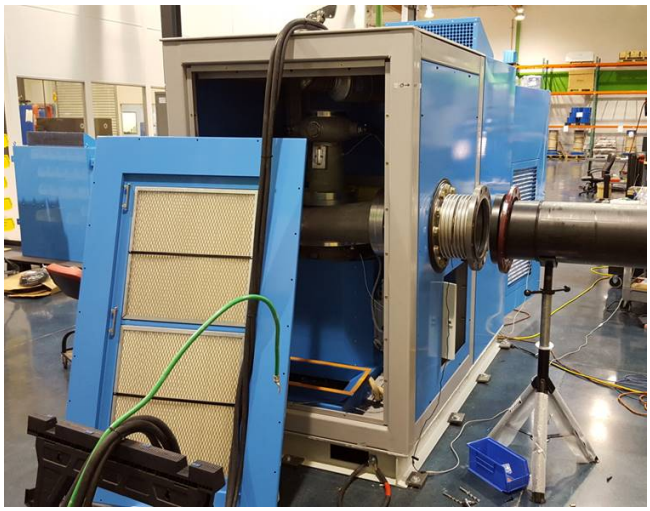

Fig. 18: Assembled turbo-aerator in cabinet with discharge pipe to the right.

8. Casing Ping Test

It is important to evaluate the casing structural natural frequencies. These must be included in the controller software if the natural frequency is in the system operating speed range. A ping test of the casing is required for this purpose. Twelve accelerometers were used to capture casing motion during a number of ping tests performed using an impact hammer. Six of the accelerometers were placed on the venturi and volute as shown in Fig. 19. The other six were placed on the motor housing as shown in Fig. 20.

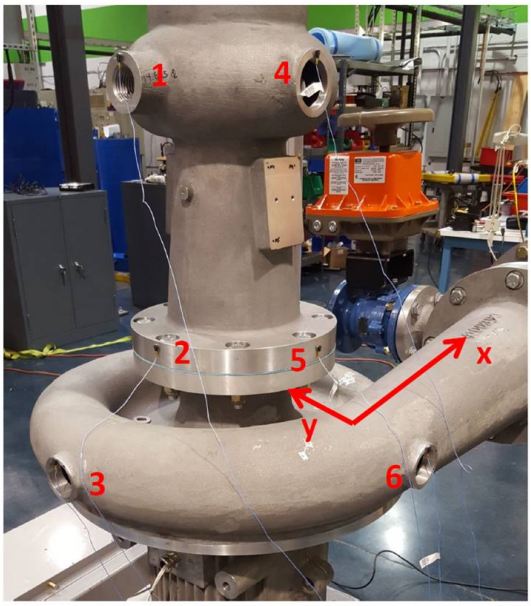

Fig. 19: Accelerometers mounted to venturi and voulte for ping test to determine structural natural frequencies.

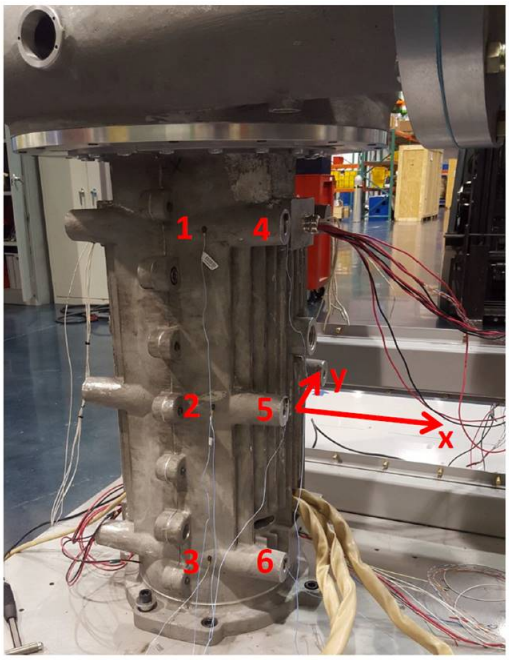

Fig. 20: Accelerometers mounted to motor casing for ping test to determine structural natural frequencies.

The volute/motor casing ping test results are shown in Fig. 21 for the x-direction, oriented in the direction of the the volute discharge, and in Fig. 22 for the y-direction, perpendicular to the x-direction. The rotor was not rotating when the ping tests were done.

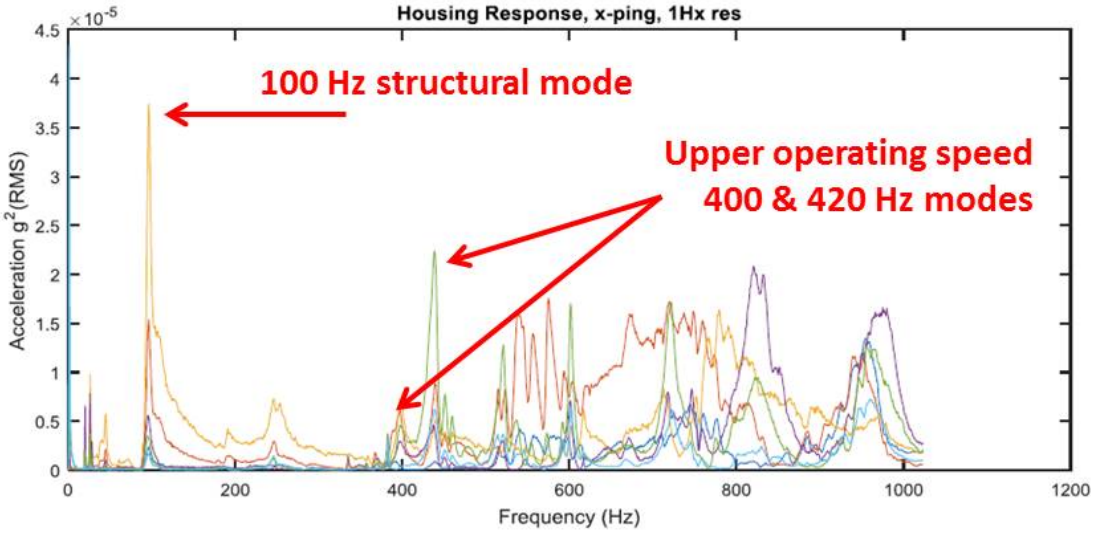

Fig. 21: Ping test results in x-direction of core machine casing with amplitude and frequency.

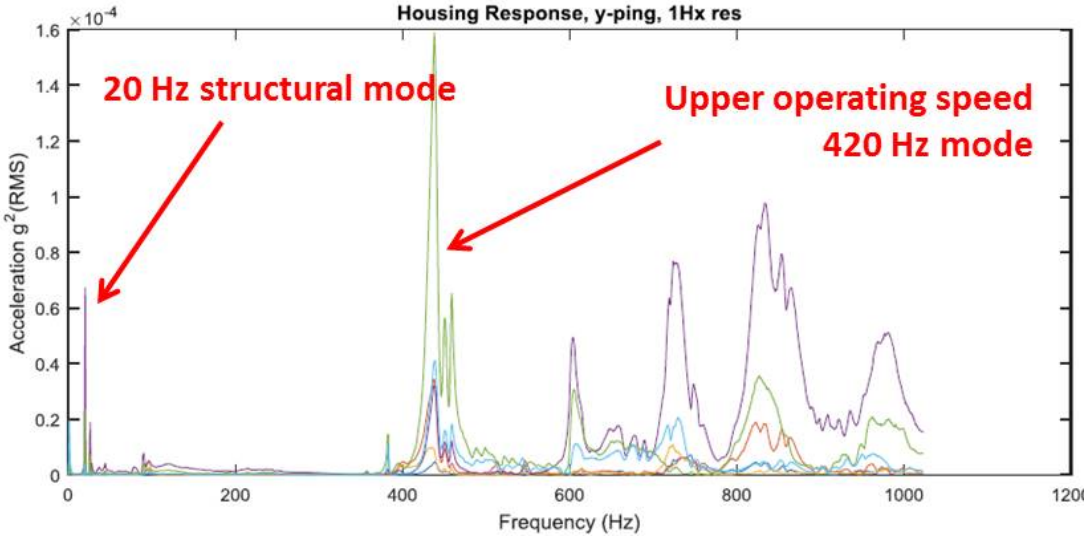

Fig. 22: Ping test results in y-direction of core machine casing with amplitude and frequency.

Two measured low frequency peaks occur in the x-direction- a small peak at 20 Hz (1,200 rpm) and a much larger one at 100 Hz (6,000 rpm), as shown in Fig. 21. These two peaks are well below the lowest operating speed of 300 Hz (18,000 rpm), so they are not very important and are not taken into account by the AMB controller. Another couple of peaks were found in the x-direction- a small peak at 400 Hz (24,000 rpm) and a larger peak at 420 Hz (25,200 rpm). These peaks are near the maximum operating speed of 416 Hz (25,000 rpm), thus, notch filters have to be introduced into the controller at these frequencies to avoid exciting them.

In the y-direction, there is a low frequency peak at approximately 20 Hz (1,200 rpm) but no significant peak at 100 Hz. There is a large peak near the operating range at approximately 420 Hz (25,200 rpm). This large peak at 420 Hz also requires a notch filter in the controller.

9. AMB Controller Hardware System

A general block diagram of the AMB controller is shown in Fig. 23. It shows the digital controller, the power amplifiers, rotor-AMB dynamics (including the rotor and AMB properties) and position sensors. A disturbance model, representing external forces transmitted to the magnetic bearings, is also included. A much more detailed control block diagram is shown in Fig. 24.

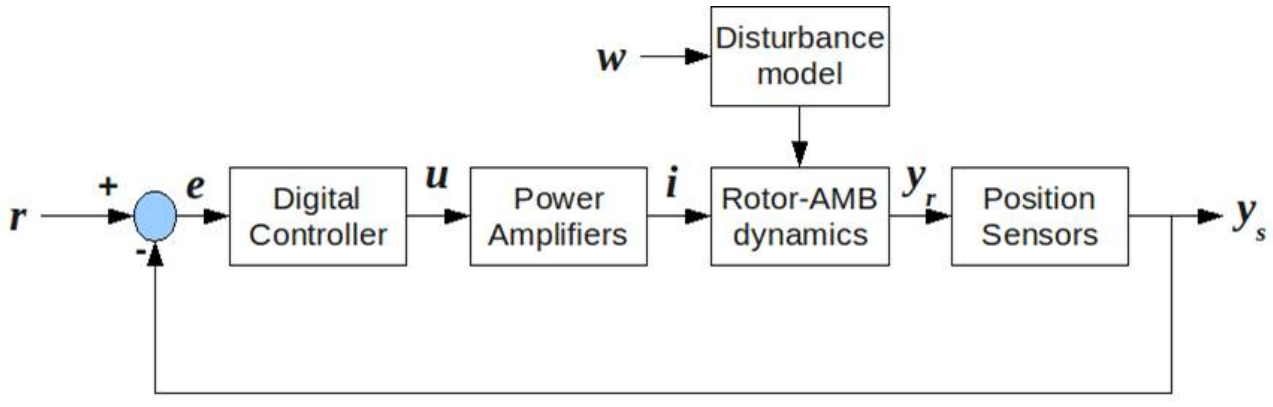

Fig. 23: Control block diagram for AMB control.

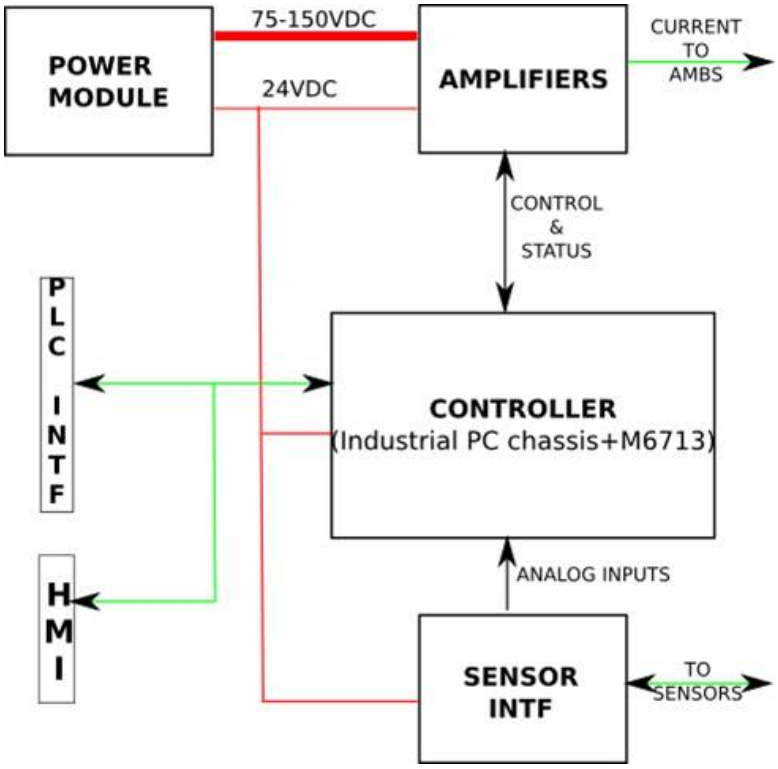

Fig. 24: Block diagram of digital control system hardware with computation module (DSP), control interface board, sensor interface boards, power amplifier module containing amplifier boards, and power supply.

A photograph of the AMB digital control board is shown in Fig. 25. It is an M6713 powerful floating point processor from Innovative Integration with 16 analog inputs and 16 analog outputs. High sample rates of up to 20 kHz are achievable. Two power amplifiers per control axis are necessary for powering the AMBs. These are amplifiers are rated at 25 A peak current and 12.5 A continuous current. The supply voltage is 40-175 VDC. These amplifiers are commonly used in brushed motor systems.

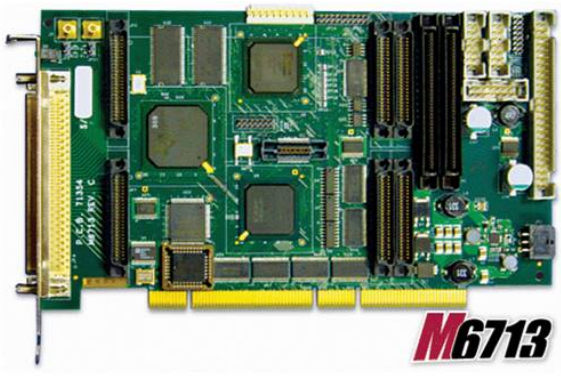

Fig. 25: Digital control board used in AMB control.

10. Control Algorithm Objectives

The control system objectives include stability, performance, and robust performance. These categories are now explained in more detail.

The controller stability is measured by the output sensitivity functions, as indicated by API Standards. The sensitivity function must have amplitude less than 3.0 (9.5 dB) for class A operation. What this means in terms of rotor dynamic properties is that each of the rotor modes are within the control bandwidth.

The measured output sensitivity function amplitude and phase angle for the upper magnetic bearing in the x-direction is shown in Fig. 26. The measured output sensitivity function for the y-direction result is presented in Fig. 27. Above 267 Hz, the output sensitivity functions are well below 9.5 dB so the AMB system has class A operation.

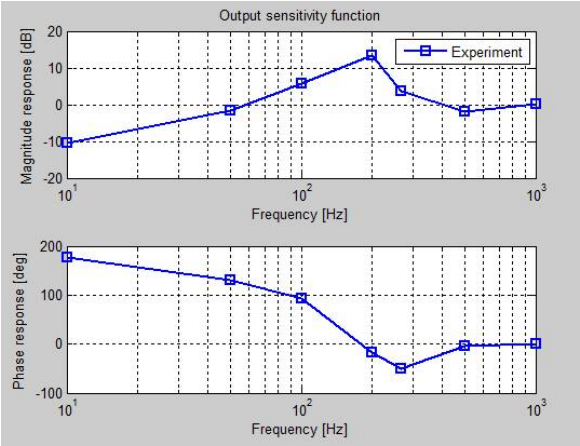

Fig. 26: Measured sensitivity function for the upper radial AMB in the x-direction.

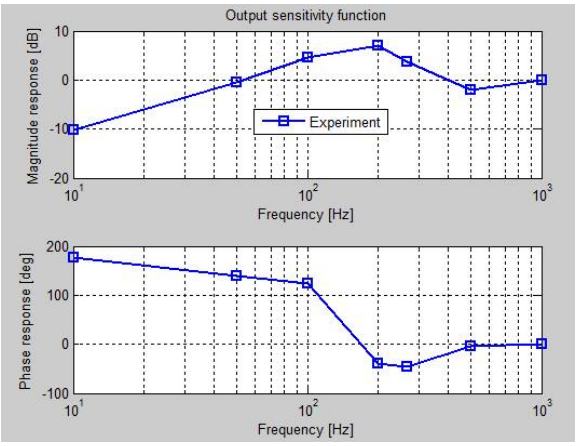

Fig. 27: Measured sensitivity function for the upper radial AMB in the y-direction.

The measured lower radial bearing output sensitivity function in the x-direction is given in Fig. 28 and in the y-direction in Fig. 29. Both of these sensitivity indicate the AMB system class A operation.

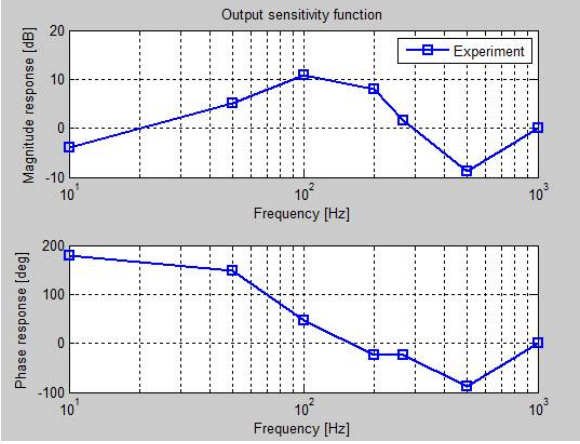

Fig. 28: Measured sensitivity function for the lower radial AMB in the x-direction.

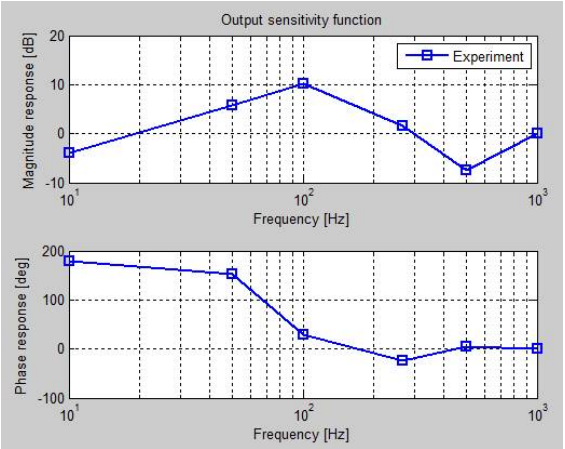

Fig. 29: Measured sensitivity function for the lower radial AMB in the y-direction.

In this rotor, the two rotor modes of interest are both rigid body modes. Also, the controller must reject external disturbances entering the plant, including sensor or other noise, static loads, and dynamic loads.

The controller performance objective is to minimize the rotor displacement at all times. The vertical load is primarily the steady state gravity load which is easily controlled. The axial control current is shown in Fig. 30. The radial bearings are subject to unbalance response loads. The rotor orbits and control currents are shown in Fig. 30.

As the rotor increases in speed, the unbalance forces dominate the vibration. The turbine motor end maximum amplitude of vibration is +/- 30 microns in the y-direction and +/- 13 microns in the x-direction. The turbine end maximum control current is +/- 8 A. At the motor end bearing, the maximum orbit amplitude of motion is +/- 15 microns in the y-direction and +/- 8 microns in the x-direction and the control current is +/- 8 A.

The vibration amplitude is controlled by an unbalance rejection, with results as shown in Fig. 30. The turbine motor end maximum amplitude of vibration is +/- 60 microns in the y-direction and +/- 23 microns in the x-direction. The

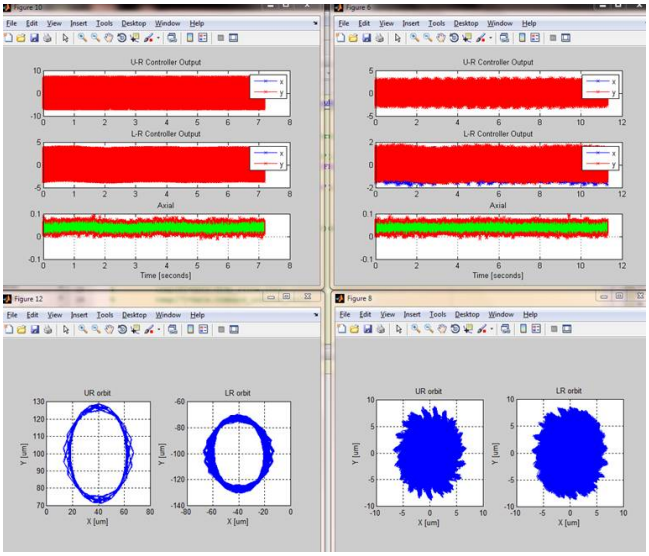

Fig. 30: Control currents and rotor orbits during typical operation.

turbine end maximum control current is +/- 3.5 A. At the motor end bearing, the maximum orbit amplitude of motion is +/- 25 microns in the y-direction and +/- 23 microns in the x-direction and the control current is +/- 1.8 A.

11. Auxiliary Bearing Design and Rotor Drop Modeling

It is very important that an auxiliary bearing system be designed for the AMB system. This allows for the auxiliary bearing to act as the protective system to ensure safe operation in the event of loss of power to the AMB system. The bearing selected is an angular contact bearing with silicon nitride ceramic balls, one piece inner ring, cageless design, and outer ring airgap from Cerobear. The outer ring airgap is typically set to one half of the AMB airgap. The auxiliary bearing diagram is shown in Fig. 31.

Fig. 31: Angular contact auxiliary ball bearing with silicon nitride ceramic balls and cageless construction.

12. Auxiliary Bearing Design and Rotor Drop Modeling

The turbo-aerator magnetic bearing system was designed and constructed as shown in the paper. The rotor has been successfully levitated and tested at this point. The thrust and radial magnetic bearings have performed as designed, levitating the rotor under gravitational load vertically and unbalance forces radially. The measured sensitivity functions are less than 9.5 dB for class A operation as indicated in ISO and API standards.

References

Fittro R. L., Baun, D. O., Maslen, E. H. and Allaire, P. E., Calibration of an 8-pole planar radial magnetic actuator, ASME Journal of Engineering for Gas Turbines and Power (1997).

Li, G., Lin, Z., Allaire, P., Huang, B., Jiang, W., Zorzi, E. and Bartlett, R., Stabilization of a high speed rotor with active magnetic bearings by a piecewise mu-synthesis controller, Proceedings of 6th International Conference on Magnetic Suspension Technology, Torino, Italy (2001).

Hu, T., Lin, Z and Allaire, P. E., Power-loss reduction by optimizing current allocation in magnetic bearings, 8th International Symposium on Magnetic Bearings, Japan (2002), pp. 169-174.

Li, G., Lin, Z., Allaire, P. and Luo, J., Modeling of high speed flywheel control test rig with active magnetic bearings, ASME Journal of Vibration and Acoustics, Vol.128, No.3 (2006), pp. 269-281.

Li, G., Lin, Z. and Allaire, P., Robust optimal balancing of high-speed machinery using convex optimization, ASME Journal of Vibration and Acoustics, Vol.130, No.3 (2008), pp. 1-11.

Mushi, S., Lin, Z., Allaire, P. E. and Evans, S., Aerodynamic cross-coupling in a flexible rotor on magnetic bearings: control design and implementation, Proceedings of the 11th International Symposium on Magnetic Bearings, Nara, Japan, August 26-29 (2008).

Yoon, S., Lin, Z., Allaire, P. E. and Lim, K. T., On the control of compressor using AMB actuation, Proceedings of the 11th International Symposium on Magnetic Bearings, Nara, Japan, August 26-29 (2008).

Huang, D., Fujimura, P., Allaire, P., Lin, Z. and Li, G., Constrained balancing of two industrial rotor systems: least squares and min-max approaches, Shock and Vibration, Vol.16, No.1 (2009), pp. 1-12.

Yoon, Y., Lin, Z., Goyne, C. and Allaire, P. E., Control of compressor surge with active magnetic bearings, 49th IEEE Conference on Decision and Control, Atlanta, Georgia (2010).

Dimond, T. W., Allaire, P. E., Mushi, S. and Lin, Z., Modal tilt/translate control and stability of a rigid rotor on active magnetic bearings, ASME Journal of Dynamic Systems, Measurement, and Control, (2011).